

Global and Local Mechanical Properties and Microstructure of Friction Stir Welds with Dissimilar Materials and/or Thicknesses

AMIR ABBAS ZADPOOR, JOS SINKE, and RINZE BENEDICTUS

This article studies the properties of a wide range of friction-stir-welded joints with dissimilar aluminum alloys or thicknesses. Two aluminum alloys, namely, 2024-T3 and 7075-T6, are selected for the study and are welded in ten different combinations of alloys and thicknesses. The welding parameters are optimized for each configuration, and a systematic study of the effects of material and thickness combinations on the microstructural features, global and local mechanical properties, and fracture mechanisms of the welds is carried out. It is shown that dissimilar alloys are extruded into each other, the texture is heterogeneous in the weld zone, and that there is no significant diffusion of alloying elements between the alloys. For most configurations, the local and global mechanical properties decrease as the thickness ratio increases. The local yield strength and plasticity parameters substantially vary next to the weld centerline, hence requiring their implementation in finite element method (FEM) models. Machining to obtain a constant thickness significantly influences the mechanical properties of the welds. The fracture mechanism is found to be a mixture of ductile and brittle fractures and to qualify as “quasi-cleavage.”

DOI: 10.1007/s11661-010-0403-3

© The Author(s) 2010. This article is published with open access at Springerlink.com

I. INTRODUCTION

TAILOR-MADE Blanks (TMBs) are sheet metals with possibly different thicknesses or materials that are joined prior to forming. The possibility of having different thicknesses and materials in a single assembly facilitates optimal distribution of material and results in effective and lean joints. Although TMBs have found numerous applications in the automotive industry, their applications are limited in the aircraft industry. That is because the high welding temperatures of fusion welding adversely affect the mechanical properties of precipitation-hardened aluminum alloys. New techniques such as machining,^[1] adhesive bonding,^[2,3] and alternative welding methods such as friction stir welding (FSW) have been suggested for production of TMBs in the aircraft industry.

In FSW, welding temperatures are well below the melting point,^[4] hence minimizing the adverse effects. The microstructure and, thus, the mechanical properties of sheets are nevertheless affected by the welding process.^[4] FSW blanks exhibit highly heterogeneous microstructural features^[5] and mechanical properties.^[6] The link between heterogeneous microstructure and

heterogeneous mechanical properties as well as the plasticity features of FSW TMBs must be known, because any application of the technology requires availability of such data as input for material selection, structure design, and manufacture planning.

There has been a vast body of research addressing the different aspects of FSW blanks including some studies of FSW blanks with dissimilar materials or different thicknesses. A summary of the studies on dissimilar-material FSW is presented in Table 24 of Reference 4. For some representative samples of the more recent studies of FSW with dissimilar materials, see References 7 through 11. There has also been considerable recent interest in FSW with dissimilar thicknesses (*e.g.*, References 12 through 15). Very limited knowledge of FSW blanks with simultaneously dissimilar alloys and thicknesses is available in the open literature. The main purpose of this article is to provide an integrated study of the different types of FSW TMBs and to contribute toward understanding how the thickness and material difference affect the microstructure and global and local mechanical properties of FSW TMBs. An extensive test matrix comprising ten different configurations (Table I) is considered. The designed test matrix allows for the study of not only the independent effects of dissimilar thickness and dissimilar alloy but also their coupled effects. Three different thicknesses of 2024-T3 and 7075-T6 sheets are used for welding. For each welded series, a parametric study is conducted to optimize the welding parameters. This is an important step to make the welds from different configurations comparable and to isolate the effects of the welding procedure from those of the TMB design parameters to the maximum possible extent. The microstructural features and the global and local

AMIR ABBAS ZADPOOR, Assistant Professor, formerly with the Materials Innovation Institute (M2i) and the Faculty of Aerospace Engineering, Delft University of Technology, is with the Faculty of Mechanical, Maritime, and Materials Engineering, Delft University of Technology. Contact e-mail: a.a.zadpoor@tudelft.nl JOS SINKE, Assistant Professor, and RINZE BENEDICTUS, Professor, are with the Faculty of Aerospace Engineering, Delft University of Technology, Delft 2629HS, The Netherlands.

Manuscript submitted September 15, 2009.

Article published online September 22, 2010

Table I. The Properties of the Base Metals

Number	Material	t (mm)	σ_y (MPa)	σ_{max} (MPa)	ϵ_{Fmax} (pct)	K (MPa)	n
i	2024-T3	2.0	418 ± 2	580 ± 3	18.2 ± 0.1	913 ± 12	0.27 ± 0.00
ii	2024-T3	1.2	388 ± 0	539 ± 0	12.3 ± 0.3	700 ± 5	0.13 ± 0.00
iii	2024-T3	2.5	370 ± 2	576 ± 2	14.8 ± 0.6	791 ± 2	0.16 ± 0.00
iv	7075-T6	2.0	533 ± 2	651 ± 2	11.2 ± 0.2	773 ± 3	0.08 ± 0.00
v	7075-T6	1.2	557 ± 1	655 ± 2	10.2 ± 0.4	778 ± 3	0.08 ± 0.00
vi	7075-T6	2.5	554 ± 1	649 ± 1	10.2 ± 0.1	761 ± 2	0.07 ± 0.00

mechanical properties of the welds as well as their fracture mechanism are presented. The grain morphology, material mixing and chemical composition, and qualitative evolution of the texture due to FSW have been studied. Although some researchers have previously studied the local mechanical properties of FSW blanks,^[6,16,17] the local mechanical properties of the welds with different materials or different thicknesses have not been studied yet. Furthermore, not enough data are available in the open literature for numerical simulation of the forming processes and formability prediction of FSW TMBs. Important examples of such data are the strain hardening exponents, strength coefficients, and anisotropy parameters. Zadpoor *et al.*^[18] have already shown that the implementation of the mechanical properties of the different weld zones is crucial for accurate finite element method (FEM) modeling of FSW TMBs. The data presented in this study partially fill the gap. The fracture surfaces of the welds are inspected with SEM, and the fracture mechanism is discussed.

II. MATERIALS AND METHODS

A. Welding Procedure

The welds were produced at the research facility of the European Aeronautic Defense and Space (EADS) Company in Germany using a fully-controlled three-axis Cartesian FSW machine (ESAB Superstir FSA, Ottobrunn, Germany). The rolling direction of the sheets was parallel with the welding direction. Two different welding angles were used. The first welding angle, α , was the angle of the welding tool with the blanks in the direction of welding. The second welding angle, θ , was the angle of the tool with the workpiece in the direction perpendicular to the welding direction, as suggested by Fratini *et al.*^[12] It was used to compensate for the thickness difference when two sheets with dissimilar thicknesses were welded. An extensive parametric study was conducted to optimize the weld parameters as well as possible. The set of parameters consisted of the rotational speed, welding feed, inclination angle (θ), pin/shoulder diameters, and pin location in the cases where the thicknesses were different. The experiments carried out during the parametric study showed that the best welds are obtained when the stronger (thicker) material is placed at the advancing side. As for the position of the pin, it was revealed that the best results are obtained when the pin is shifted by 0.8 mm toward the thinner material. The final weld parameters are listed in Table II. The welds were naturally aged for a minimum of 45 days

after welding to ensure optimal and consistent mechanical properties.

B. Experiments

Metallographic samples were cut from the welds. They were mounted, ground, and polished up to 1 μm and electrochemically etched using a Baker etching agent (5 g HBF₄ 35 pct dissolved in 200 mL distilled water). Optical microscopy with digital camera, polarization, and $\frac{1}{4}$ lambda filters was used to visualize the microstructure. The grain morphology was studied using the optical microscope. The texture pattern was studied qualitatively taking advantage of the fact that the grains with different crystallographic orientations reflect the polarized light differently.

The mechanical properties of the base metals were characterized through a dedicated series of tensile testing (Table I). The dimensions of the tensile test specimens were according to the full-size standard specimen described in the ASTM standard E8 (metric). The tensile test specimens of the welds were prepared in two different conditions: as welded and machined. For the as-welded (AW) specimens, the weld samples were edge milled to the standard full-size dog-bone shape, as specified in ASTM E8, without any modification through the thickness. The machined (M) specimens were not only milled at the edges to the same dog-bone shape, but also shaved on top to reach a uniform thickness all over the specimen, thereby eliminating the geometric effects of thickness difference. The weld line was perpendicular to the loading direction for all the specimens. The specimens were tested at a constant deformation rate of 2 mm/min. A digital image correlation (DIC) system was used to measure the local mechanical properties of the M's. Therefore, the top surface of the specimens was covered by a speckle ink pattern. A high-resolution digital camera capable of automatically photographing the area of interest at a frame rate of up to 7.5 Hz was used to record the morphology of the ink pattern during the tensile testing. The local strain values were calculated by correlating the random patterns in the successive images using a DIC program. The timing of the camera was synchronized with the timing of the test machine. Having the strain values and the corresponding force values, the local stress-strain curves were established. The offset yield strengths were calculated for each local stress-strain curve. The Hollomon's strain hardening equation ($\sigma = K\epsilon^n$) was fitted to the plastic part of the local stress-strain curves to determine the local values of the

Table II. The Global Mechanical Properties of the Base Metals and FSW as Well as Welding Parameters and Failure Locations

Number	I	II	α	θ	d	D	ω	v	F	σ_y			σ_{max}			ϵ_{Fmax}			Failure Location								
										AW	M	AW	M	AW	M	AW	M	AW	M	AW	M	AW	M	Zone	Side	Zone	Side
1	i	i	2	0	12	3	1200	400	8.0 to 9.9	360 ± 4	336 ± 4	555 ± 19	434 ± 9	19.2 ± 2.8	12.3 ± 4.6	WN/TMAZ	—	WN/TMAZ	—								
2	i	ii	2	2.1	6	3	1500	150	3.5	315 ± 6	315 ± 20	569 ± 18	428 ± 17	13.3 ± 1.9	9.9 ± 0.6	WN/TMAZ	II	TMAZ	II								
3	iii	i	2	2.1	6	3	1500	150	3.7	389 ± 2	347 ± 4	476 ± 35	444 ± 4	8.9 ± 2.4	8.1 ± 0.1	WN/TMAZ	II	WN/TMAZ	I								
4	iv	iv	2	0	12	5	400	100	12.0	490 ± 9	418 ± 8	551 ± 4	522 ± 8	9.5 ± 0.3	7.8 ± 0.2	HAZ	—	HAZ	—								
5	iv	v	2	2.1	13	5	400	100	9.5 to 10.5	440 ± 3	408 ± 12	449 ± 3	514 ± 15	4.0 ± 0.4	7.2 ± 0.2	HAZ	II	HAZ	I								
6	vi	iv	2	2.1	13	5	400	100	9 to 10	444 ± 1	393 ± 11	510 ± 4	502 ± 12	5.9 ± 0.0	7.9 ± 0.1	HAZ	II	HAZ	II								
7	i	iv	2	0	13	3	1200	400	9.5	365 ± 2	353 ± 7	528 ± 5	504 ± 16	13.0 ± 0.7	12.8 ± 0.7	HAZ	I	HAZ	I								
8	i	v	2	2.1	13	5	400	100	9 to 10	437 ± 2	339 ± 6	480 ± 4	534 ± 5	3.9 ± 0.0	7.3 ± 0.2	HAZ	II	HAZ	I								
9	vi	i	2	2.1	13	5	400	100	10 to 11	361 ± 2	349 ± 6	454 ± 5	433 ± 13	7.5 ± 0.1	7.4 ± 0.4	HAZ	II	HAZ	II								
10	iii	iv	2	2.1	13	5	400	100	8.5 to 9.5	416 ± 4	330 ± 13	519 ± 4	468 ± 18	7.3 ± 0.1	12.1 ± 0.7	HAZ	II	TMAZ	I								

σ_y (MPa): yield strength, σ_{max} (MPa): tensile strength, ϵ_{Fmax} (pct): strain at maximum force, α (deg): weld angle, θ (deg): inclination angle, d (mm): shoulder diameter, D (mm): pin diameter, ω (min^{-1}): rotational speed, v (mm/min): travel speed, F (kN): tool force, I: first material, II: second material, AW: as-welded condition, M: machined condition, WN: weld nugget, HAZ: heat-affected zone, and TMAZ: thermomechanically affected zone.

strength coefficient, K , and the strain hardening exponent, n . The fracture surfaces of the tensile test specimens were inspected using scanning electron microscopy (SEM). The chemical compositions of the alloys were examined using the energy dispersion spectrometry element mapping and spot measurement techniques. The backscatter mode of SEM was used to identify particles and intermetallics.

III. RESULTS AND DISCUSSION

A. Microstructural Features

The two dissimilar alloys that are joined through FSW experience significant thermomechanical evolution including high strain rate vortices at elevated temperatures and (possibly) local melting, which may result in their chemical mixing. There are two questions to be answered. First, does FSW result in chemical mixing? Second, do the alloying elements diffuse during FSW? Figure 1(a) depicts the microstructure of the stirring zone of a representative weld (configuration 8). As is clear from this figure and was observed for the other configurations as well, there is a clear division line between the two alloys, implying that the alloys were not chemically mixed. This is in line with the findings of previous studies in which no or very limited chemical mixing was found.^[19-21] Figure 1(b) presents the EDS

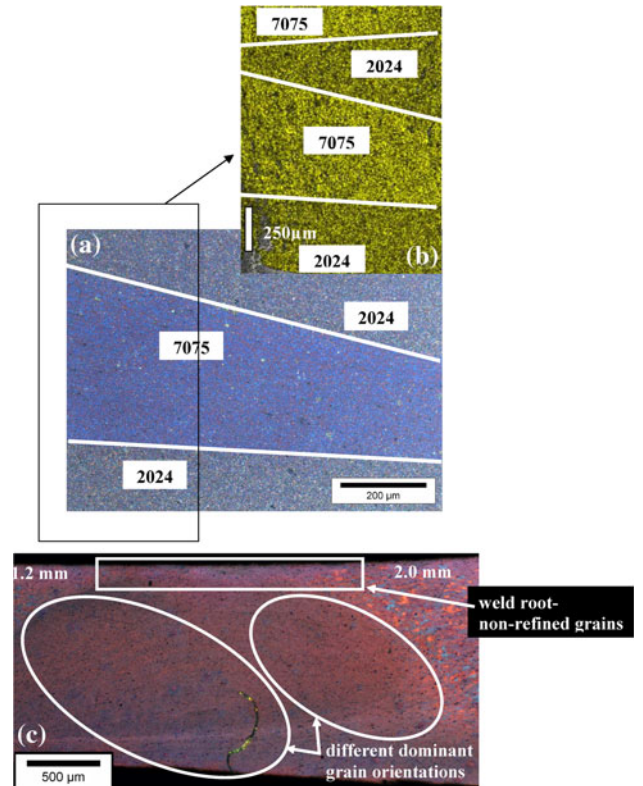


Fig. 1—(a) Microstructure and (b) EDS Zn element mapping of the WN of a sample weld from configuration 8, and (c) the microstructural features of the stirring zone of a sample weld from configuration 2. The magnifications of subfigures (a), (b), and (c) are 100, 70, and 25 times, respectively.

mapping of Zn for the same representative weld. The 7075-T6 alloy has a significant amount (5.1 to 6.1 pct) of Zn, but the Zn content of 2024-T3 is negligible (<0.254 pct). Therefore, Zn element mapping can distinguish between the two alloys. The boundaries of Zn-rich zones are clearly matching the observed microstructural lines, meaning that the dissimilar alloys are not chemically mixed. Indeed, FSW has been suggested to work as a localized cold-working process combining conventional metal working zones of preheat, plastic (initial deformation), extrusion, forging, and cool-down.^[22] The dissimilar alloys are merely extruded into each other, as can also be seen in Figures 3(c) and (f).

As for the diffusion of the alloying elements of dissimilar alloys into each other, there is a disagreement in the literature. While the studies of FSW of 7075 and 6065^[23] and 5083 and 6061^[24] suggest that there is no diffusion, a study of the FSW of steel and 6013 showed slight diffusion from steel to 6013.^[25] Moreover, the chemical compositions reported for the welding of 2024-T3 and 7075-T6 show incomplete diffusion of the elements between the two alloys.^[19]

The thermomechanical mixing of the weld material during the welding process not only extrudes the alloys and brings them close to each other, but also increases the temperature and velocity and lowers the viscosity, thereby increasing the diffusion rate. Whether significant diffusion takes place during FSW depends on two parameters: temperature and dwell time. These two parameters are dependent on the welding parameters (the geometry of the welding tool, rotational speed, *etc.*) and the mechanical properties of the materials during FSW. The dwell time is longer if the travel speed of the tool is lower. The alloys used in this study are high strength aerospace alloys, the pressure of the welding tool is significant, and the travel speed is sometimes quite low. Nevertheless, the EDS analysis of the welds with dissimilar alloys showed that there is no significant diffusion of alloying elements from one alloy to the other. Some spot measurements of the Mg, Zn, and Cu contents along a line perpendicular to the boundary between 2024-T3 and 7075-T6 in Figures 1(a) and (b) (and some similar figures) were carried out (not presented). They showed a sudden jump from the chemical composition of one alloy to that of the other alloy without any sizable diffusion from one material to the other. A first approximation of the diffusion length ($= 2\sqrt{Dt}$) can be obtained using the Arrhenius equation ($D = D_0 \exp(-Q/RT)$) and the pre-exponential diffusion factors ($D_0 = 0.6 \times 10^{-6} - 2.0 \times 10^{-5} \text{ m}^2/\text{s}$) and activation energies ($Q = 100$ to 120 kJ/mole) gathered in Reference 26 for diffusion of Zn, Cu, and Mg in polycrystalline fcc Al. The peak temperatures ($T = 550 \text{ K}$ to 700 K ($277 \text{ }^\circ\text{C}$ to $427 \text{ }^\circ\text{C}$)) and dwell times ($t = 10$ to 30 seconds) were estimated from the graphs presented in Reference 27 and its cited references. The diffusion depth, accordingly, was estimated to be between 0.1 and $1.6 \text{ }\mu\text{m}$. These values should be used just as an order-of-magnitude indication, because some of the assumptions behind the equations do not hold in FSW. The estimated range of diffusion length is too small to be detected by EDS accurately.

Figure 1(c) depicts the microstructure of the stirring zone of a sample weld from configuration 2. The grains are highly refined in the weld nugget (WN) due to dynamic recrystallization (DRX). The classic onion rings structure can be detected in the figure. A larger version of Figure 1(a) as well as an additional supporting figure is presented in an electronic supplement accompanying this article. The structure of onion rings is clearer in those figures. Interestingly, the dominant grain structure on the advancing side (2024-T3, 1.2 mm) is different from the one on the retreating side (2024-T3, 2 mm). This has to do with the different rotation fields of the shear component of the texture on the advancing and retreating sides. The texture of the WN is measured to be mainly composed of shear component.^[28] On the advancing side, the rotation field created by the pin rotates the shear component in the counter-clockwise direction, while the shear component is rotated in the clockwise direction on the retreating side.^[28] Therefore, the plastic deformation imposes preferred grain orientation on either side. For configurations 1-3, 4, and 7, the preferred orientation gradually changes from the advancing side toward the retreating side, because individual rings within the onion rings structure gradually change in texture progressing from the advancing side toward the retreating side. In the literature, the differences between the textures at the advancing and retreating sides are normally explained based on the differences in material flow caused by pin rotation.^[5,29] It is shown that the texture poles rotate in the direction of tool rotation while progressing from one side toward the other.^[29] The same effect is expected to be observed for all configurations. However, other factors such as the texture change caused by shoulder^[29] can change the expected change of texture as going from one side to the other. This is particularly important for configurations with dissimilar thicknesses and dissimilar alloy, because the effects of shoulder are different for those configurations. For the other configurations (configurations 5, 6, and 8 through 10), there were two different texture types, each of which related to one of the base metals (Figures 1(a), 3(c), and 3(f)). As pin partially penetrates into the materials, the grains are not well refined in the weld root (Figure 1(c)), meaning that the weld may be weaker in the root. This is reflected in the lower hardness of the weld root compared to the weld toe and its immediate neighborhood.^[30]

Figure 2 presents the morphology and chemical composition of the particles within the different zones of a sample weld from configuration 8. The high temperatures of FSW result in dissolution, coarsening, and re-precipitation of the precipitates.^[4] As is clear from Figures 2(a) through (c), there are a relatively large number of large particles in the WN and the heat-affected zones (HAZs) of both materials. The particles tend to be larger (up to $25 \text{ }\mu\text{m}$) in the HAZs compared to the WN (up to $10 \text{ }\mu\text{m}$). That may be due to the coarsening of the precipitates and could be the reason why the lowest strengths are measured within the HAZ. The number of smaller particles ($500 \text{ nm} - 1 \text{ }\mu\text{m}$) is significant in the WN and the HAZ of the 2024 side, but there are not as many such particles in the HAZ of the

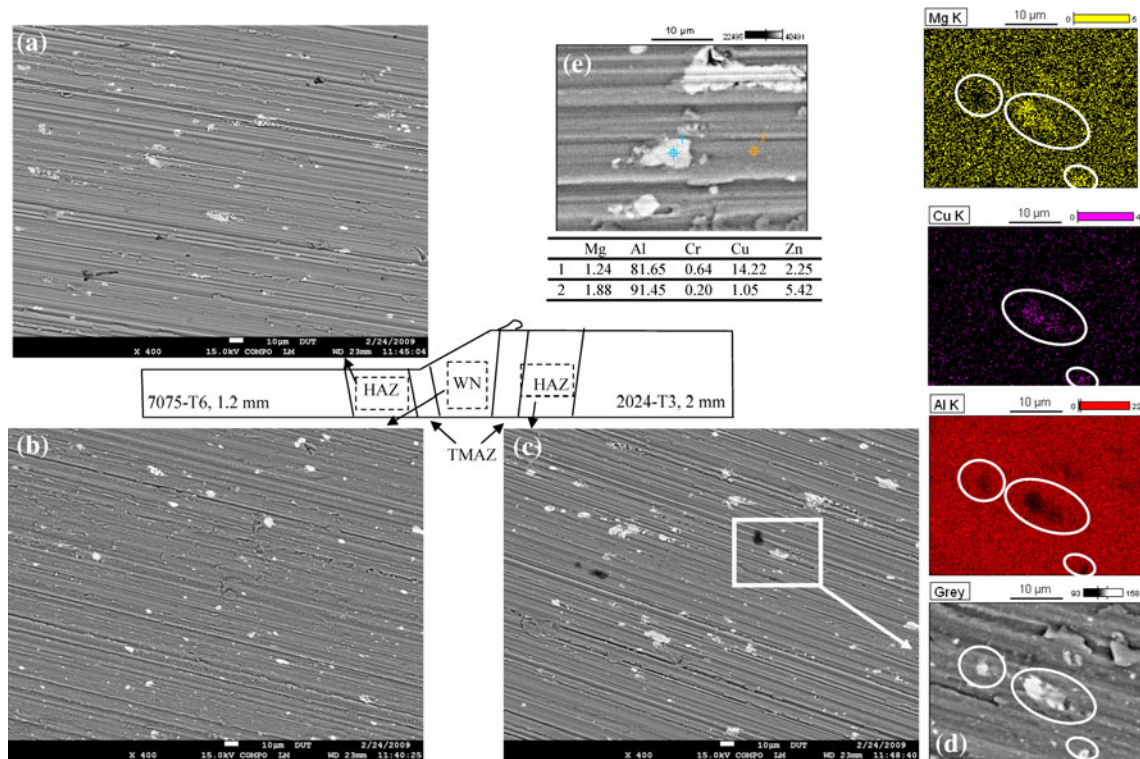


Fig. 2—Backscatter images of the HAZ of the (a) 7075 and (b) 2024 sides of sample specimens from configuration 8 (c) along with its WN. Two magnified views of the HAZ of the (d) 2024 side and (e) 7075 side are also provided. The EDS element mapping and spot element analysis are carried out for subfigures (d) and (e), respectively.

7075 side. Figure 2(d) presents the EDS element maps for a few large particles in the HAZ of the 2024 side and shows that the particles are rich in Cu and Mg. In Figure 2(e), the EDS spot measurement technique is used to compare the composition of two points: a point in the matrix and a point within a large particle. The point within the particle is clearly much richer in Cu and lacks Zn. These large intermetallics can potentially limit the plastic deformation by stopping various active slip systems.

Figure 3 consists of a schematic drawing of a typical weld accompanied by some sample micrographs representing various locations within the weld zone. The microstructural morphology of the base metals (Figure 3(a)) was consistent with the usual morphology of cold-rolled sheets with grains elongated along the rolling direction. Figure 3(b) presents the grain morphology in the HAZ of a sample right next to the thermomechanically affected zone (TMAZ). One can see that the grain size is comparable to that of the base metal; yet, the aspect ratio of the grains is somewhat smaller due to the high temperatures experienced during FSW. The mixing of two different alloys in the WN of the welds with dissimilar materials and dissimilar thicknesses is represented in Figure 3(c), where it can be clearly seen that the two alloys are extruded into each other and form a WN with strongly heterogeneous texture. The 2024-T3 alloy is extruded into 7075-T6 and has its own distinctive grain orientation. The onion ring structure is still detectable in the 7075 portion of the nugget. Within the 7075 portion, one can also see the difference between the dominant grain orientations of

the advancing and retreating sides. The highly deformed grains in the TMAZ zone are shown in Figure 3(d). Although the size of the grains is preserved, they are curled in accordance with the circular strain field created by the tool.

It was found that there is a sudden change of grain orientation on both sides of the WN in the dissimilar-thickness configurations (Figures 3(e) and (f)) such that the area with the suddenly changed texture surrounds the WN. Larger versions of Figures 3(e) and (f) as well as an additional supporting figure are presented in the electronic supplement accompanying this article. The larger versions show the sudden change of texture more clearly. Figure 3(g) shows the highly refined grains of weld burr that are refined through DRX. In summary, FSW causes significant change in the chemical composition and grain orientation through the thickness.

B. Global Mechanical Properties

The global mechanical properties of the studied FSW TMBs as well as their failure locations are presented in Table II. One can see that in most cases the thermomechanical evolution during the welding degrades the mechanical properties of the welds. Table III presents the differences between the mechanical properties of the welds and those of the base materials as well as the differences between the mechanical properties of the AW and M specimens. The yield and tensile strengths of the welds are in most cases less than the yield and tensile strengths of either base metal. In a few cases, the yield or

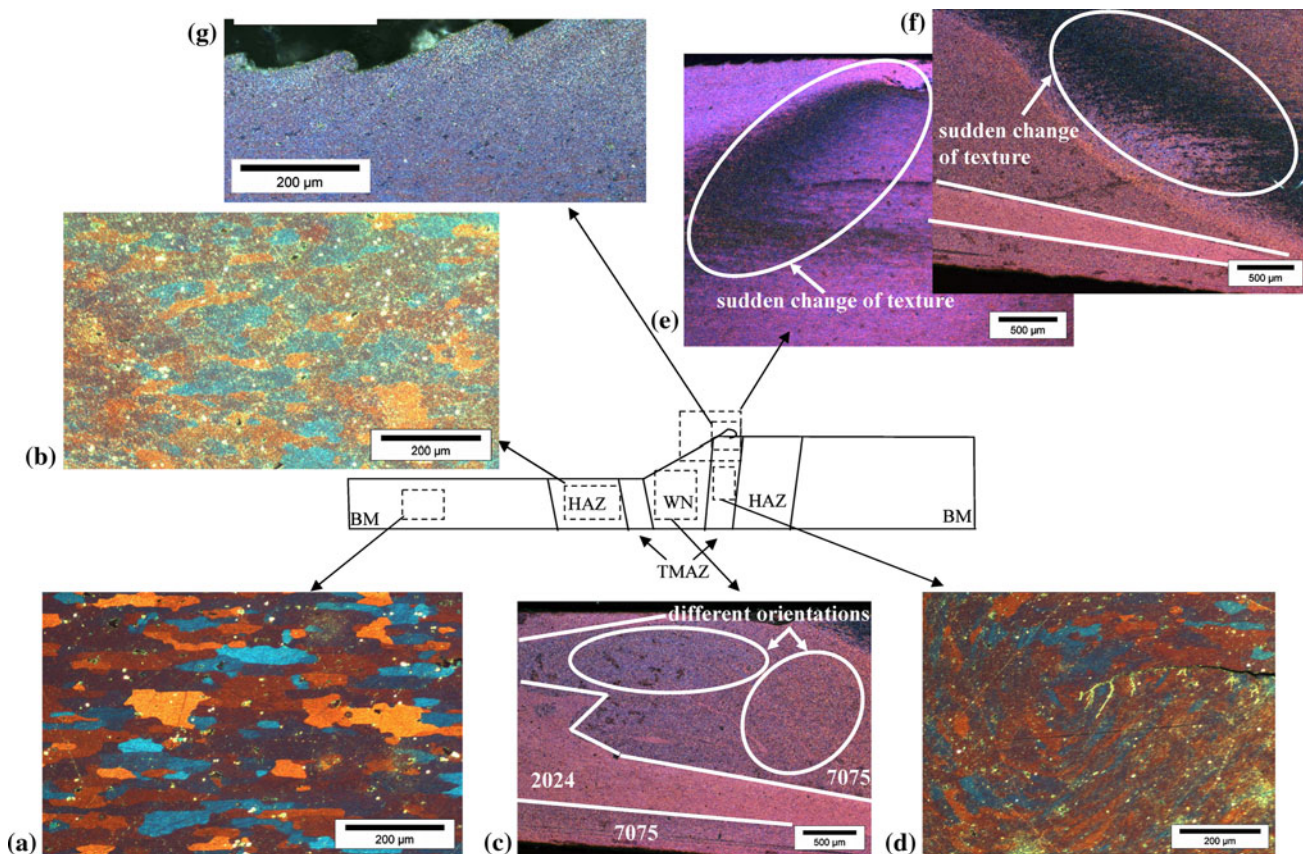


Fig. 3—Schematic representation of the different zones of the welds with dissimilar thicknesses or dissimilar alloys. Subfigures (a) through (g) depict some samples of the microstructural features observed for different weld configurations. (a) Base metal from configuration 2 (magnification 100 times). (b) HAZ from configuration 2 (magnification 100 times). (c) Stirring zone from configuration 9 (magnification 25 times). (d) TMAZ from configuration 2 (magnification 100 times). (e) and (f) WN and TMAZ from configuration 9 (magnification 25 times), and (g) weld burr from configuration 5 (magnification 100 times).

Table III. The Differences between the Global Mechanical Properties of the AW and M Specimens and Those of the Base Metals; the Differences between the Mechanical Properties of the AW and M Specimens are Presented as Well; Each Cell of the Table Contains the Absolute Difference Value (Bold) Followed by the Percentage Value (Italic)

No.	σ_y (MPa)					σ_{max} (MPa)					ϵ_{Fmax} (Pct)				
	I-W	I-M	II-W	II-M	W-M	I-W	I-M	II-W	II-M	W-M	I-W	I-M	II-W	II-M	W-M
1	58,14	82,20	58,14	82,20	24,7	25,4	146,25	25,4	146,25	121,22	-1,0,-5	5,9,32	-1,0,-5	5,9,32	6,9,36
2	103,25	103,25	73,19	73,19	0,0	11,2	152,26	-30,-6	111,21	141,25	4,9,27	8,3,46	-1,0,-8	2,4,20	3,4,26
3	-19,-5	23,6	29,7	71,17	42,1	100,17	132,23	104,18	136,23	32,7	5,9,40	6,7,45	9,3,51	10,1,55	0,8,9
4	43,8	115,22	43,8	115,22	72,5	100,15	129,20	100,15	129,20	29,5	1,7,15	3,4,30	1,7,15	3,4,30	1,7,18
5	93,17	125,23	117,21	149,27	32,7	202,31	137,21	206,31	141,22	-65,-14	7,2,64	4,0,36	6,2,61	3,0,29	-3,2,-80
6	110,20	161,29	89,17	140,26	51,1	139,21	147,23	141,22	149,23	8,2	4,3,42	2,3,23	5,3,47	3,3,29	-2,0,-34
7	53,13	65,16	168,32	180,34	12,3	52,9	76,13	123,19	147,23	24,5	5,2,29	5,4,30	-1,8,-16	-1,6,-4	0,2,2
8	-19,-5	79,19	120,22	218,39	98,2	100,17	46,8	175,27	121,18	-54,-11	14,3,79	10,9,60	6,3,62	2,9,28	-3,4,-87
9	193,35	205,37	57,14	69,17	12,3	195,30	216,33	126,22	147,25	21,5	2,7,26	2,8,27	10,7,59	10,8,59	0,1,1
10	-46,-12	40,11	117,22	203,38	86,1	57,10	108,19	132,20	183,28	51,10	7,5,51	2,7,18	3,9,35	-0,9,-8	-4,8,-66

I-W: The difference between the first base metal and the AW specimens, I-M: the difference between the first base metal and M's, II-W: the difference between the second base metal and the AW specimens, II-M: the difference between the second base metal and the M's, and W-M: the difference between the AW and M specimens.

tensile strength(s) of the weld is less than that of a base metal but more than that of the other base metal. Similarly, the ductility of the welds is in most cases less than that of either base metal. However, the ductility is in some cases more than that of a base metal, although

still less than the other. As is clear from this table, the yield strengths of the different configurations decrease in the range of 7 to 35 pct for AW specimens and in the range of 6 to 39 pct for M specimens. The range of the decrease of the ultimate strength is 2 to 31 pct for AW

specimens and 8 to 33 pct for M specimens. In the case of the strain at maximum stress, the decreases are in the range of 0 to 79 pct for AW specimens and 0 to 60 pct for M specimens. Two trends emerge from the values presented in Table III. First, the yield strengths of the M specimens are for many configurations (all except configuration 3) worse than those of the AW specimens, although the difference is not always significant. The difference between the ultimate strength of the M and AW specimens is only significant in the case of configurations 1, 2, and 10. Second, the loss of ductility (in terms of percentage) is in many cases more than the loss of strength (in terms of percentage). This is an important point given the fact that the sheets will be plastically formed after FSW.

There are four fundamental differences between AW and M specimens. First, there are local stress concentrations due to the roughness of the weld toe in the AW specimens, which are removed in the M specimens by machining. Second, stress concentrations occur at the transition line from one thickness to the other for the welds with dissimilar thicknesses. Again, it is removed in the M specimens, where the upper surface is milled to obtain a uniform thickness throughout the specimen. Third, there is a gradual thickness change in the AW specimens with dissimilar thicknesses (Figure 3), meaning that the thickness of the WN is somewhat larger than the thinner base metal. Therefore, the stress in the WN/TMAZ is less than in the thinner base metal. If the weakest point happens to be within the WN/TMAZ, the failure would be earlier in the M specimens, where the thickness of the WN/TMAZ is the same as the thinner base metal. In the fourth place, the penetration of the pin into the material is partial, meaning that the weld root is not as well consolidated as the rest of the weld (Figure 1(c)). Therefore, the mechanical properties of the weld root are not as good as the rest of the weld cross section. Through thickness measurement of the hardness has shown the minimum hardness at the weld root.^[30] The machining process removes some well-consolidated material from the top side of the weld and, thus, enhances the ratio of the weld root material to the well-consolidated material. Among these four mechanisms, the first two work toward lowering the mechanical properties of the AW specimens in comparison with the M specimen. The last two mechanisms work toward heightening the mechanical properties of the AW specimens. The second and third mechanisms are active only for the configurations with dissimilar thicknesses, whereas the first and last mechanisms are active for all configurations. The differences between the mechanical properties of the AW and M specimens depend on the balance of these four active mechanisms. Table III presents the differences between the mechanical properties of the AW and M specimens. As is clear from this table, the yield strength of the AW specimens is always higher than that of the M specimens. The same holds for the ultimate strength, except for configurations 5 and 8. Configurations 5 and 8 are the ones with the highest thickness ratio ($r = 1.7$). Stress concentration due to the change of the thickness is the greatest for these two configurations. That may be the reason why the ultimate

strength and the strain at maximum stress are better for the M specimens from these two configurations. As for the strain at the maximum stress, the M specimens deform to a larger extent only in the case of configurations 5, 6, 8, and 9, all of which have a thickness ratio greater than 1. One has to note that these are just static properties and the trends could change in the case of dynamic loading, where the local and global stress concentrations are more relevant.

The effects of the thickness ratio on the mechanical properties can be studied by comparing the configurations presented in Table II. The strain at maximum stress for the configurations with dissimilar thicknesses is less than that of the same-thickness configurations. This holds not only for the AW specimens, but also for the M specimens in which the stress concentration caused by the thickness difference does not play a role. A stronger statement can be made for the dissimilar-thickness configurations from 7075-T6 (configurations 4 through 6) and the dissimilar-thickness dissimilar-alloy configurations (configurations 7 through 10). For these two cases, the strain at maximum stress decreases as the thickness ratio increases. The welding parameters of configurations 4 through 6 are almost the same. The only difference is in shoulder diameter of configuration 4, which is 12 mm instead of 13 mm. Therefore, there should not be much difference in terms of the welding parameters for these three configurations. For configurations 7 through 10, the welding parameters are the same for configurations 8 through 10 and only the welding parameters of configuration 7 are different. For this configuration (configuration 7), the welding (travel) speed is greater than the other three configurations. The ratio of rotational speed to travel speed is lower for this configuration. Higher weld speed and lower ratio of rotational speed to travel speed means lower heat input. That may be a contributing factor to the fact that elongation of specimens from configuration 7 is more than those from the other configurations (*i.e.*, configurations 8 through 10). Therefore, the formability of FSW TMBs at least for some configurations decreases as the thickness ratio increases, meaning that production of the structural parts out of FSW TMBs with high thickness ratio is more difficult. As for the yield strength and tensile strength, they generally tend to be lower for the configurations with dissimilar thicknesses. Although the statement holds firmly for the 7075-T6 configurations (configurations 4 through 6), it is not without exception for the 2024-T3 configurations (configurations 1 through 3) and dissimilar-alloy configurations (configurations 7 through 10).

The configurations with dissimilar alloys can be divided into two groups. The first group includes the configurations for which the thickness of the 2024-T3 sheet is the same or smaller than the 7075-T6 sheet, namely, configurations 7 and 9. The second group includes configurations 8 and 10 for which the thickness of the 7075-T6 is less than that of the 2024-T3 sheet. Table II shows that failure always takes place in the 2024-T3 side for the first group, which is due to the lower strength of 2024-T3 in the HAZ zone as compared with the local strength of 7075-T6 in the HAZ zone

(compare the local mechanical properties of different configurations in Section III–C). For the second group, failure takes place at the 7075-T6 side for the AW specimens, but moves to the 2024-T3 side once the thickness is leveled by machining. The mechanical properties of the second group are similar to those of the corresponding 7075-T6 configurations (configurations 4 through 6). The same type of comparison cannot be done between the first group and 2024-T3 configurations (configurations 1 through 3), because the failure location of the specimens from 2024-T3 configurations are different from the failure location of the specimens from the first group.

Interestingly, there are some differences between the mechanical properties of configurations 9 and 10. Although the same alloys are welded in these two configurations, the thicknesses of the sheets are different. After machining, the thicknesses are the same and one therefore expects the mechanical properties of the M specimens from configurations 9 and 10 to be similar. However, the elongation of the M specimens from configuration 10 is significantly higher than that of the M specimens from configuration 9. The yield and ultimate strengths of the M specimens from configuration 10 are also higher than those of the M specimens from configuration 9, although to a lesser extent. Even though the failure location is different for these two configurations (the HAZ for configuration 9 vs the TMAZ for configuration 9), one can still try to explain their differences in terms of heat input. That is because the TMAZ and HAZ are adjacent zones and are close in terms of temperature. The major difference between the HAZ and TMAZ is the mechanical effects that are present in the TMAZ but are absent in the HAZ. The heat input of FSW can be estimated as^[31]

$$Q = \frac{4\pi^2\alpha\mu PNR^3}{3V} \quad [1]$$

where the heat input efficiency, α , and friction coefficient, μ , can be assumed to be similar for configurations 9 and 10. Table II shows that the travel speed, V , rotational speed, N , and shoulder diameter, R , are the same for both configurations. However, the tool pressure, P , is higher for configuration 9, because it is the harder 7075-T6 that has to be squeezed by the shoulder to make the gradual thickness change (from one material to the other) possible. Since the other parameters (including the specific heat of the materials) tend to be similar, the temperature would be higher for configuration 9 as compared to configuration 10, meaning that the 2024-T3 alloy is subject to a more severe overaging and precipitation coarsening in the case of configuration 9.

One should note that the difference in the welding parameters of the different configurations can also play a major role in determining the mechanical properties of the resulting welds. Some of the effects of the welding parameters are reflected in the heat input (Eq. [1]). However, the welding parameters may have other effects that cannot be understood without measurement of other involving factors such as the temperature profile.

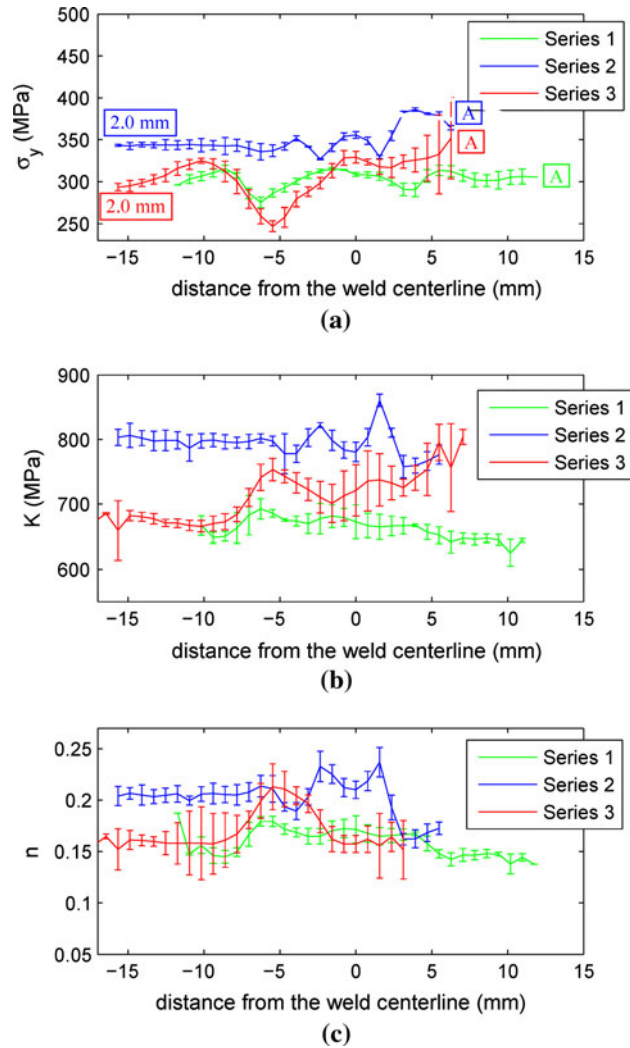


Fig. 4—(a) Local yield stress, (b) strength coefficient, and (c) strain hardening exponent for configurations 1 through 3. The advancing side of each configuration is marked using an “A.”

C. Local Mechanical Properties

The local mechanical properties including the yield strength, strength coefficients, and strain hardening exponents are presented in Figures 4 through 6. Table IV lists the maximum and minimum values of the local mechanical properties as well as the differences between the maxima and the minima. The local mechanical properties of the FSW blanks are not widely available, and the values presented in Figures 4 through 6 are helpful in the FEM modeling of FSW blanks. One can see that the difference between the maximum and minimum values of the local yield strength is between 14 to 46 pct of the average of the maximum and minimum values. The difference is between 10 and 62 pct for the strength coefficient and between 13 and 71 pct for the strain hardening exponent. Since the FSW blank will be ultimately formed into structural parts, it is important to be able to build accurate FEM models of the FSW blanks. On the one hand, the level of the difference between the maximum and minimum values is so large that one cannot be

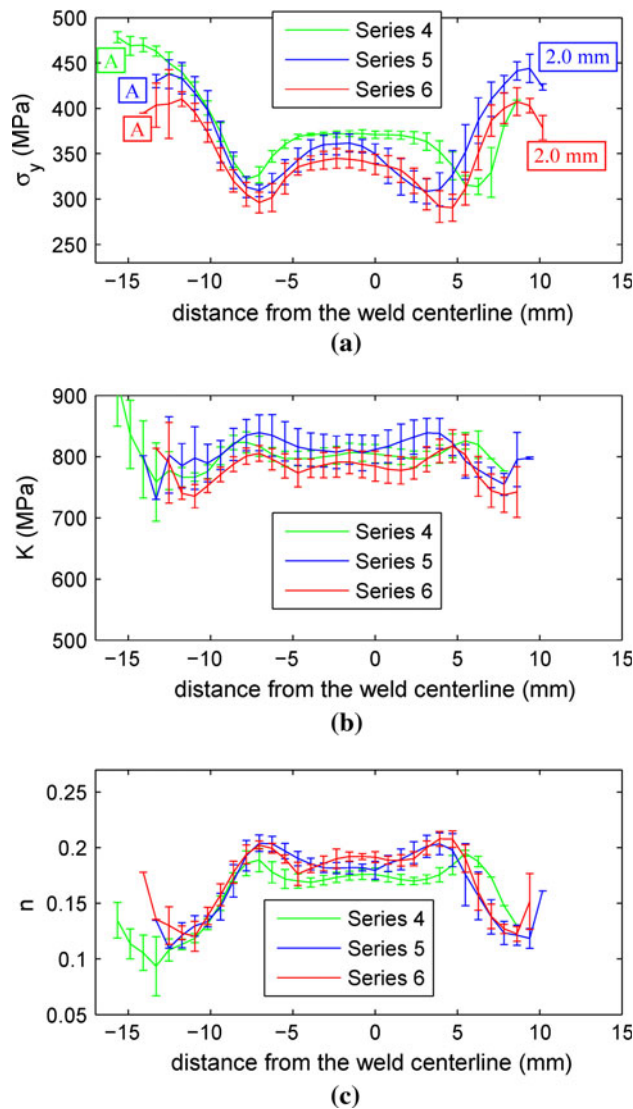


Fig. 5—(a) Local yield stress, (b) strength coefficient, and (c) strain hardening exponent for configurations 4 through 6. The advancing side of each configuration is marked using an “A.”

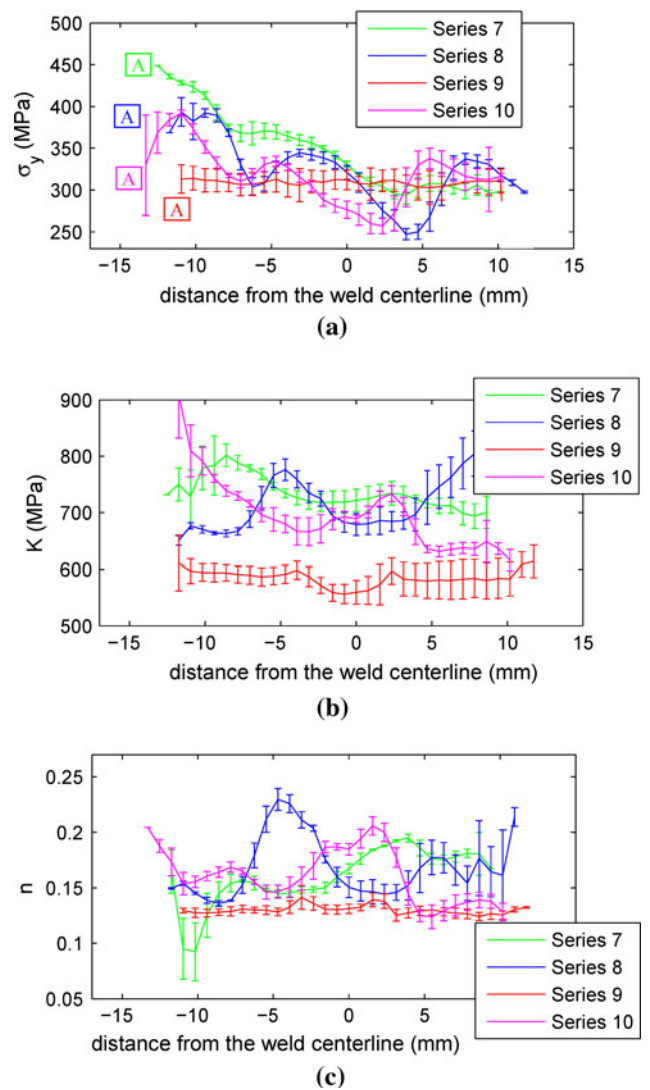


Fig. 6—(a) Local yield stress, (b) strength coefficient, and (c) strain hardening exponent for configurations 7 through 10. The advancing side of each configuration is marked using an “A.”

Table IV. The Maximum and Minimum Values of the Local Mechanical Properties of the Welds from Different Configurations as Well as the Differences between the Maxima and Minima

Series		1	2	3	4	5	6	7	8	9	10
σ_y	max	315	386	352	478	444	410	449	393	314	392
	min	275	327	247	314	308	290	294	247	259	257
	Δ	40,14 pct	59,17 pct	105,35 pct	165,42 pct	135,36 pct	120,34 pct	155,42 pct	146,46 pct	55,19 pct	135,42 pct
K	max	693	861	804	923	839	817	802	975	614	1172
	min	625	758	660	759	731	735	694	650	556	616
	Δ	68,10 pct	103,13 pct	144,20 pct	164,20 pct	109,14 pct	82,11 pct	108,14 pct	325,40 pct	58,10 pct	556,62 pct
n	max	0.187	0.237	0.213	0.195	0.204	0.208	0.195	0.230	0.141	0.206
	min	0.138	0.162	0.152	0.093	0.110	0.120	0.092	0.136	0.124	0.124
	Δ	0.050, 31 pct	0.075, 38 pct	0.061, 34 pct	0.101, 70 pct	0.094, 60 pct	0.087, 53 pct	0.103, 71 pct	0.094, 51 pct	0.017, 13 pct	0.082, 50 pct

Max: maximum value of the local mechanical properties depicted in Figs. 4 through 6. Min: minimum value of the local mechanical properties depicted in Figs. 4 through 6. Δ : The difference between the maximum and minimum values expressed both as the absolute value and percentage of the average (of the maximum and minimum values). The absolute value is presented first and is separated with a comma from the percentage value. σ_y (MPa): yield strength, K (MPa): strength coefficient in the Hollomon's strain hardening law, and n : strain hardening exponent in the Hollomon's strain hardening law.

certain about the accuracy of the FEM models without implementing the local mechanical properties in the model. On the other hand, the implementation results in more computationally expensive simulations that may or may not be justified by the extra accuracy obtained due to the implementation of the local mechanical properties. Zadpoor *et al.* have addressed this problem for FSW blanks with the same thicknesses and the same materials and have shown that the implementation of the local mechanical properties substantially improves the capability of FEM models in predicating the strain distribution and springback behavior of the FSW.^[18]

The difference between the maximum and the minimum values of the tensile strength are 14 to 35 pct for the 2024-T3 series and 35 to 42 pct for the 7075-T6 series. This is due to the natural aging of the 2024-T3 that recovers the strength of the locally-heated areas, whereas the artificially aged 7075-T6 is not able to recover the strength to a comparable extent. Therefore, determination of the local mechanical properties is even more important for artificially aged alloys. The differences between the maximum and minimum values of tensile strength are quite high in the case of dissimilar-alloy configurations that are due to the large difference between the mechanical properties of 2024-T3 and 7075-T6.

Comparing Figures 4(a) and 5(a), one can see that the yield strength profiles are different for 2024-T3 and 7075-T6. While the 7075-T6 configurations exhibit a smooth distribution of the yield strength around the weld centerline with two minima on the either side of the weld, the yield strength profile is less smooth in the case of 2024-T3 configurations and includes several minima and maxima. Previous studies have shown that FSW has a major impact on the distribution of the dislocation density and creates a nonhomogenous distribution of the dislocation density.^[32,33] It is known that in 2024-T3, dislocations can strongly interact with the precipitates and act as preferred location for the nucleation of precipitates.^[34,35] Since the dislocations are heterogeneously distributed, the precipitate distribution is heterogeneous as well. That may be the reason why several maxima and minima exist in the yield strength profile of 2024-T3. Indeed, thermophysical modeling of the FSW of 2024 has shown that if the effects of the dislocation density are left out of the model, the predicted hardness profile is essentially similar to that of 7075.^[36] Several other factors such as different temperatures and cooling rates (that could cause coarse precipitation) and different precipitation sequences in two alloys may be playing a role and further study is needed to determine which of these mechanisms is playing a major role. The different FSW parameters that are used for 2024-T3 and 7075-T6 may also have an impact on the difference between the distributions of the mechanical properties.

Even though there are some local differences between the welds from different configurations, the pattern of variations in the mechanical properties is more or less similar in all configurations. The highest values of the local yield strength are measured away from the weld centerline, where the thermal influence of FSW is minimal. The mechanical properties gradually decrease

as one progresses toward the weld centerline. The minimum values of the yield strength were measured around the weld centerline. It is suggested by several researchers that this high level of softening around the weld centerline is caused by dissolution and coarsening of the hardening precipitates during the welding process.^[4,37,38] The lower values of the local yield strength and higher values of the local strain hardening exponent (Figures 4 through 6) indicate that the material close to the weld centerline is softer and undergoes much more deformation than the material present in the other areas of the gage length of the tensile test specimens. The mechanical properties of the softened region (mostly WN) increase over time due to re-precipitation of the precipitating elements.^[4,21] The minima of the yield strength occur in the areas where there is lack of the supersaturation of precipitating elements (*i.e.*, HAZ),^[4,21] meaning that re-precipitation is not possible. Even for the configurations for which the sheet at the advancing side is similar to the one at the retreating side, the local mechanical properties are asymmetric around the weld centerline (Figures 4 through 6). The tensile strength tends to be higher on the advancing side than on the retreating side. This trend has been observed in other studies as well, *e.g.*, References 38 through 41, and may be due to the different deformation histories on the advancing and retreating sides. The material on the advancing side is influenced to a greater extent by the vortex velocity field. That is because the circumventing and rotational velocity fields have different directions on the retreating side but are of the same direction on the advancing side. Therefore, the straining and grain refinement is more severe on the advancing side.^[41] According to the Hall–Petch relationship, this results in higher yield strengths.

The effect of the thickness ratio on the local yield strength (Figures 4(a) through 6(a)) is different for the 2024-T3 configurations as compared to the 7075-T6 configurations and dissimilar-alloy configurations. While the levels of the yield strength of the 7075-T6 and dissimilar-alloy configurations are relatively close to each other and tend to be higher for the same-thickness cases, the reverse holds for the 2024-T3 configurations. This may be described in terms of the heat input during the FSW estimated with Eq. [1]. The equation can be simplified if the friction coefficient and efficiency can be assumed to be similar:

$$Q = A \frac{FNR}{V}, \quad A = \frac{4\pi\alpha\mu}{3} \quad [2]$$

Replacing for the parameters from Table II, the heat input of the 2024-T3 configurations can be calculated as $Q_1 = 153A$, $Q_2 = 105A$, and $Q_3 = 111A$, where the subscript denotes the configuration number. For the 7075-T6 configurations, the rotational speed and travel speed are the same and can be incorporated into A to give $A' = 4\pi\alpha\mu N/V$. The heat inputs of the 7075-T6 configurations can then be compared using only the tool force and shoulder diameter (Table II): $Q_4 = 144A'$, $Q_5 = 124A'$, and $Q_6 = 124A' - 130A'$. As is clear from the calculated heat inputs, in the case of the 2024-T3 configurations, the required heat input increases as the

thickness ratio increases. This may cause higher temperatures, more severe dissolution and coarsening of the precipitates, and thus, degradation of the mechanical properties. In the case of the 7075-T6 configurations, the heat input is similar for the three configurations and the local mechanical properties are close. However, one should note that Eq. [1] is suggested for the same-thickness configurations. In the case of dissimilar alloys, the shoulder must deeply penetrate into the material with larger thickness, and this may result in higher heat input. That may be the reason why in the case of the harder 7075-T6 alloy, the level of the yield strength slightly decreases as the thickness ratio increases. Moreover, the heat capacities of sheets with different thicknesses are different. As a result, the same amount of heat input does not necessarily result in the same temperature profile.

The hardness profiles are often used to give a measure of the local mechanical properties of FSW. The hardness measurements are often carried out locally, for example, along the centerline of the cross section. Since there is a significant change of the hardness values through the thickness,^[30] one cannot know *a priori* whether the local hardness measurements can give a reasonably valid picture of the local mechanical properties of the entire cross section. The hardness profiles of the 2024-T3 configurations measured along the centerline of the cross section were published in our previous article.^[21] Comparing Figures 4 through 6 with the previously published hardness profiles of the same welds, one can see that there are two fundamental differences between them. First, the hardness profiles suggested that after natural aging, the yield strength of the WN of 2024 is almost the same as that of the base metal. Figures 4 through 6 show that the peak yield strengths in the WN are well below those of the base metals, if the entire weld is considered. Second, the hardness profiles suggest a trend for the dependency of the local mechanical properties upon the thickness ratio that is contradicting the trend suggested by the direct measurement of the local mechanical properties of the entire weld section. Therefore, the local measurement of the hardness profiles may not give a reasonably accurate picture of the distribution of the mechanical properties around the weld centerline, and one has to resort to techniques such as DIC for that.

One of the mechanisms limiting the formability of FSW blanks is strain localization. According to the Marciniak–Kuczynski theory of localization bifurcation,^[42] the strain localization phenomenon is controlled by the imperfection parameter defined as

$$f = \frac{K_2 t_2}{K_1 t_1} \quad [3]$$

where K_2 and t_2 are, respectively, the yield strength and thickness of the imperfection zone, and K_1 and t_1 are the nominal values of the same quantities. The theory assumes that strain localization originates from areas with smaller thickness or lower yield strength whose strain paths are always ahead of the uniform zone. The localization takes place once the ratio of the strain of

the imperfection zone to that of the strain zone approaches infinity. In the case of the FSW blanks, the variations of the local yield strength observed in Figures 4 through 6 can give rise to such imperfections and cause premature metal failure. An in-depth analysis of formability is needed to determine the relative importance of this phenomenon compared to other active failure mechanisms.

D. Fracture Mechanism

Table II shows that the fracture locations of the same-alloy configurations are either in the WN/TMAZ (for 2024-T3) or the HAZ (for 7075-T6). In the latter group, the fracture location coincides with the minima of the yield strength profile (Figure 5(a)), where the material is softened due to the dissolution and coarsening of the precipitates. In the former group, however, the yield strength of the fracture site is not necessarily the lowest (Figure 4(a)). The fracture of 7075-T6 takes place in the HAZ, is controlled by the softening of the material, and involves significant development of a localized neck. In contrast, the fracture of 2024-T3 occurs in the WN, in some cases does not exhibit significant development of a localized neck, and is hypothesized to be controlled by lack of ductility.

Some samples of the inspected fracture surfaces are presented in Figures 7 and 8. The ductile fracture mechanism is normally identified by dimples and tearing edges. The brittle fracture mechanism is identified by a relatively featureless fracture surface that may include cleavage facets, river patterns, and feather markings.^[43] For the entire weld series listed in Table I, the fracture surfaces exhibited the features of both ductile and brittle fracture mechanisms. However, there were two types of the mixture of the features of ductile and brittle fractures. In the first type, the fracture surfaces were predominantly occupied by the features of one single fracture mechanism (ductile or brittle), and the features

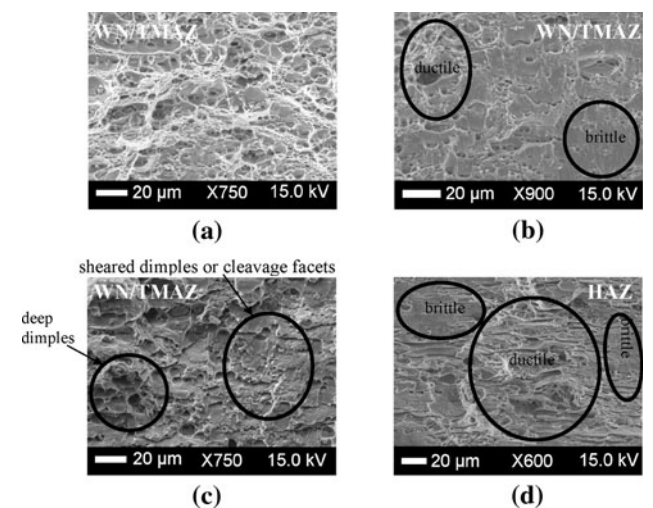


Fig. 7—Fracture surfaces of some sample welds from configurations (a) and (b) 2, (c) 1, and (d) 4.

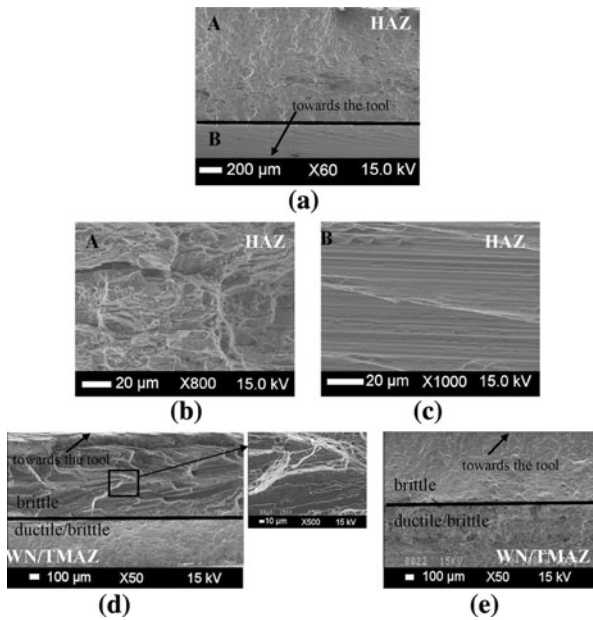


Fig. 8—(a) Overview of the fracture surface of a sample specimen from configuration 8 along with two magnified views of the regions (b) A and (c) B. Overviews of the fracture surface of two sample specimens from configurations numbers (d) 2 and (e) 3. A magnified view is provided for the brittle fracture region of the sample depicted in subfigure (d).

of the other mechanism were scattered over the fracture surface. In the second type, the fracture surface was divided into two distinct regions: one overwhelmingly exhibiting the features of brittle fracture and the other demonstrating ductile or mixed ductile/brittle fracture. Figure 7 depicts some samples of the first type and Figure 8 some samples of the second type.

Figures 7(a) and (b) show the fracture surface of a sample from configuration 2. In Figure 7(a), it can be seen that the features of ductile fracture dominate the fracture surface. Figure 7(b) presents a different part of the fracture surface of the same specimen. A mixture of the features of ductile and brittle fractures is present in this figure. The area depicted in Figure 7(b) is almost featureless with some shallow dimples and some traits resembling cleavage facets scattered throughout the surface. However, these features can be considered to be sheared dimples as well. Figure 7(c) depicts the fracture surface of a sample from configuration number 1. The fracture surface is composed of areas that clearly exhibit the features of ductile fracture such as relatively deep dimples. However, there are some other areas in this figure that can be considered to be either sheared dimples or cleavage facets. Closer examination of these features revealed that they are more likely to be sheared dimples. In this scenario, the deep dimples relate to the start of the crack. After the initial phase of crack formation, the specimen experiences overloading and the dimples are sheared. Cavaliere *et al.* observed a behavior similar to that depicted in Figures 7^[44] for same-thickness same-alloy FSWs. They concluded that the observed cleavagelike fracture is due to a nonoptimal grain structure of the recrystallized material. In this

scenario, the high strain rate acting on the material during the welding results in boundary weakening in the dynamically recrystallized zone. A possible explanation for the first type of the mixing between the features of ductile and brittle fractures is that the dislocation movement is blocked by the many intermetallics (Figure 2) that are observed in the HAZ and WN. Voids cannot nucleate and grow in the proximity of the particles, resulting in the fracture surface being divided.

Figure 8(a) gives an overview of a sample specimen from configuration 8. As is clear from this figure, the fracture surface is divided into two distinct regions with the upper one (region A, Figure 8(b)) showing a mixed ductile/brittle fracture and the lower one (region B, Figure 8(c)) not showing any sign of ductile fracture. The same kind of behavior was observed for some other configurations (Figures 8(d) and (e)). It was observed that the brittle regions (the regions similar to region B in Figure 8(c)) were on the side of the material that had been in contact with the shoulder of the tool. Moreover, the size of the brittle region was (at least in some cases) dependent on the thickness ratio and increased as the thickness ratio increased. Comparing Figures 8(d) and (e), one can see that the portion of the fracture surface showing brittle fracture is larger for configuration 2 (Figure 8(d)) for which the thickness ratio (1.7) is more than the thickness ratio (1.2) of configuration 3 (Figure 8(e)). Moreover, the division of the fracture surface was not observed in configurations for which the failure location was away from the domain of the influence of the shoulder. These three observations suggest that the creation of the brittle region may be due to the significant penetration of the tool's shoulder into the sheets. As already pointed out, the shoulder has to deeply penetrate into the thicker sheet to create the gradual thickness change. The severe plastic deformation of the top side of the sheets during the welding process could be the reason why a brittle region is formed on the side of the sheets that had been in contact with the shoulder. Xu *et al.*^[45] and Elangovan and Balasubramanian^[46] have also observed the division of the fracture surface into two regions for *same-thickness welds*. Contrary to our observations, they observed the cleavagelike fracture in the weld root and suggested that it is due to the poor consolidation of the metal at the weld root. Therefore, the thickness difference present in our experiments results in a different type of divisive feature than the one reported in the literature. Cleavagelike fracture is observed in the areas other than weld root for other fcc materials such as FSW copper.^[47,48] Liu *et al.* attributed the cleavagelike features to defect voids that were observed in their welds on the advancing side. No such defect was identified in the current study.

As fcc materials, aluminum alloys are generally considered to fail only through ductile fracture mechanism and not cleavage.^[43] This finding is because of the numerous active slip systems in fcc materials. However, cleavage is reported for fcc materials under special circumstances.^[43] As discussed earlier, there are some features in the fracture surfaces of FSW specimens that resemble the cleavage fracture. Similar results have been reported by other researchers.^[44,46,49,50] In most cases,

fracture surfaces showed the features of both ductile and brittle fractures. The term “quasi-cleavage” can be used to describe the type of fracture observed in the testing of FSW blanks. According to the *ASM Handbook of Fractography*, “quasi-cleavage fracture is a localized, often isolated feature on a fracture surface that exhibits characteristics of both cleavage and plastic deformation.”^[43] The term quasi-cleavage implies that the features of the fracture surface resemble, but are not, cleavage. Therefore, using the term quasi-cleavage for description of the mixed behavior of the fracture surfaces implies that the fracture mechanism is not necessarily changed to the low-energy fracture mechanism that propagates along well-defined low-index crystallographic directions and is known as cleavage. It is not clear if the fracture mechanism is actually changed or the features that resemble the cleavage fracture are merely signs of limited plastic deformation. It should be noted that the ideal cleavage takes place only under certain well-defined conditions such as single-crystalline microstructure and limited number of slip systems.^[43] Most of the times, there is a combination of plastic and cleavage fractures. The division line between the terms cleavage and quasi-cleavage is somewhat arbitrary.^[43]

IV. CONCLUSIONS

The microstructure and local and global mechanical properties of FSW TMBs were studied in this article. The following conclusions can be drawn from the study.

1. Dissimilar materials are merely extruded into each other, and there is no sizable diffusion of the alloying elements between the alloys and they form a WN with strongly heterogeneous texture varying both through the thickness and around the weld line. There is a sudden change of texture around the WN when thicknesses are dissimilar. Large intermetallic particles were observed in the HAZ and WN. Their different sizes and morphology differed in the different zones of the welds.
2. Although all mechanical properties degrade after FSW, ductility is influenced to a greater extent. Both high thickness ratio and through-the-thickness machining tend to adversely affect the mechanical properties. The properties of FSW with dissimilar thicknesses are close to those of the weaker alloy. Many of the trends observed for the global and local mechanical properties may be explained using the heat input estimates.
3. The local yield strength and plasticity parameters drastically vary around the weld centerline, requiring them to be implemented in the FEM models. The local properties are asymmetric around the centerline with the advancing side having higher properties.
4. The fracture mechanism of FSW TMBs was found to match the definition of quasi-cleavage fracture. Depending on the material/thickness configuration of the weld, the features of the ductile and brittle

fracture are either (1) quasi-randomly scattered over the fracture surface or (2) segregated with a sharp boundary separating the brittle fracture region from the area exhibiting ductile or mixed ductile/brittle fracture. While the brittle regions that are scattered may have been created due to the large intermetallic particles that block the dislocation movement and void nucleation and growth, the creation of the sharply separated brittle regions may be due to the deep penetration of the shoulder that is required due to the dissimilar thicknesses of the blanks.

ACKNOWLEDGMENTS

This research was carried out under Project No. MC1.05224 in the framework of the Strategic Research Programme of the Materials Innovation Institute M2i (<http://www.m2i.nl>), the former Netherlands Institute for Metals Research.

OPEN ACCESS

This article is distributed under the terms of the Creative Commons Attribution Noncommercial License which permits any noncommercial use, distribution, and reproduction in any medium, provided the original author(s) and source are credited.

ELECTRONIC SUPPLEMENTARY MATERIAL

The online version of this article (doi:[10.1007/s11661-010-0403-3](https://doi.org/10.1007/s11661-010-0403-3)) contains supplementary material, which is available to authorized users.

REFERENCES

1. A.A. Zadpoor, J. Sinke, and R. Benedictus: *J. Mater. Proc. Technol.*, 2008, vol. 200, pp. 288–99.
2. A.A. Zadpoor, J. Sinke, and R. Benedictus: *Int. J. Adhes. Adhes.*, 2009, vol. 29, pp. 558–71.
3. A.A. Zadpoor, J. Sinke, and R. Benedictus: *Mater. Des.*, 2010, vol. 31, pp. 4611–20.
4. R.S. Mishra and Z.Y. Ma: *Mater. Sci. Eng. R*, 2005, vol. 50, pp. 1–78.
5. D.P. Field, T.W. Nelson, Y. Hovanski, and K.V. Jata: *Metall. Mater. Trans. A*, 2001, vol. 32A, pp. 2869–77.
6. S. Liu and Y.J. Chao: *Mod. Sim. Mater. Sci. Eng.*, 2005, vol. 13, pp. 1–15.
7. C. Leitão, B. Emilio, B.M. Chaparro, and D.M. Rodrigues: *Mater. Des.*, 2009, vol. 30, pp. 3235–42.
8. C. Leitão, R.M. Leal, D.M. Rodrigues, A. Loureiro, and P. Vilaça: *Mater. Des.*, 2009, vol. 30, pp. 101–08.
9. P. Cavaliere, A. De Santis, F. Panella, and A. Squillace: *Mater. Des.*, 2009, vol. 30, pp. 609–16.
10. P. Venkateswaran, Z.-H. Xu, X. Li, and A. Reynolds: *J. Mater. Sci.*, 2009, vol. 44, pp. 4140–47.
11. C.Y. Lee, D.H. Choi, Y.M. Yeon, and S.B. Jung: *Sci. Technol. Weld. Join.*, 2009, vol. 14, pp. 216–20.
12. L. Fratini, G. Buffa, and R. Shivpuri: *Mater. Sci. Eng. A*, 2007, vol. 459, pp. 209–15.

13. G.J. Grant, R.W. Davies, E.V. Stephens, S. Wazny, L. Kaunitz, and D.J. Waldron: *SAE Trans.: J. Mater. Manufact.*, 2006, vol. 114, pp. 619–29.
14. M.B. Silva, M. Skjoedt, P. Vilaca, N. Bay, and P.A.F. Martins: *J. Mater. Proc. Technol.*, 2009, vol. 209, pp. 811–20.
15. K. Chung, W. Lee, D. Kim, J. Kim, K.-H. Chung, C. Kim, K. Okamoto, and R.H. Wagoner: *Int. J. Solids Struct.*, 2010, vol. 47, pp. 1048–62.
16. J. Yan, M.A. Sutton, and A.P. Reynolds: *Mater. Sci. Eng. A*, 2006, vol. 427, pp. 289–300.
17. R.W. Fonda and S.G. Lambrakos: *Sci. Technol. Weld. Join.*, 2002, vol. 7, pp. 177–181.
18. A.A. Zadpoor, J. Sinke, and R. Benedictus: *Mater. Des.*, 2009, vol. 30, pp. 1423–34.
19. S.A. Khodir and T. Shibayanagi: *Mater. Sci. Eng. B*, 2007, vol. 148, pp. 82–87.
20. H. Larsson, L. Karlsson, S. Stoltz, and E. Bergqvist: *2nd Int. Symp. on Friction Stir Welding*, Gothenburg, Sweden, 2000.
21. A.A. Zadpoor, J. Sinke, and R. Benedictus: *Mater. Sci. Eng. A*, 2008, vol. 494, pp. 281–90.
22. W.J. Arbegast: *TMS Annual Meeting*, San Diego, CA, 2003, Z. Jin, A. Beaudoin, T.A. Bieler, and B. Radhakrishnan, eds., TMS, San Diego, CA, 2003, pp. 313–27.
23. P.B. Srinivasan, W. Dietzel, R. Zettler, J.F. dos Santos, and V. Sivan: *Mater. Sci. Eng. A*, 2005, vol. 392, pp. 292–300.
24. I. Shigematsu, Y.J. Kwon, K. Suzuki, T. Imai, and N. Saito: *J. Mater. Sci. Lett.*, 2003, vol. 22, pp. 353–56.
25. H. Uzun, C.D. Donne, A. Argagnotto, T. Ghidini, and C. Gambaro: *Mater. Des.*, 2005, vol. 26, pp. 41–46.
26. Y. Du, Y.A. Chang, B. Huang, W. Gong, Z. Jin, H. Xu, Z. Yuan, Y. Liu, Y. He, and F.Y. Xie: *Mater. Sci. Eng. A*, 2003, vol. 363, pp. 140–51.
27. Y.-M. Hwang, Z.-W. Kang, Y.-C. Chiou, and H.-H. Hsu: *Int. J. Mach. Tools Manufact.*, 2008, vol. 48, pp. 778–87.
28. Y.S. Sato, H. Kokawa, K. Ikeda, M. Enomoto, S. Jogan, and T. Hashimoto: *Metall. Mater. Trans. A*, 2001, vol. 32A, pp. 941–48.
29. S. Agarwal, C.L. Briant, L.G. Hector, and Y.L. Chen: *J. Mater. Eng. Perf.*, 2007, vol. 16, pp. 391–403.
30. *Friction Stir Welding and Processing*, R.S. Mishra and W.H. Murray, eds., ASM INTERNATIONAL, Materials Park, OH, 2007.
31. Ø. Frigaard, Ø. Grong, and O. Midling: *Metall. Mater. Trans. A*, 2001, vol. 32A, pp. 1189–1200.
32. L.E. Murr, G. Liu, and J.C. McClure: *J. Mater. Sci. Lett.*, 1997, vol. 16, pp. 1801–03.
33. W.B. Lee and S.B. Jung: *Mater. Lett.*, 2004, vol. 58, pp. 1041–46.
34. R. Ferragut and A. Somoza: *Phys. Status Solidi A*, 1999, vol. 175, pp. R1–R2.
35. C. Genevois, D. Fabrègue, A. Deschamps, and W.J. Poole: *Mater. Sci. Eng. A*, 2006, vol. 441, pp. 39–48.
36. H.R. Shercliff, M.J. Russell, A. Taylor, and T.L. Dickerson: *Mecan. Indus.*, 2005, vol. 6, pp. 25–35.
37. S. Benavides, Y. Li, L.E. Murr, D. Brown, and J.C. McClure: *Scripta Mater.*, 1999, vol. 41, pp. 809–15.
38. Y. Li, L.E. Murr, and J.C. McClure: *Mater. Sci. Eng. A*, 1999, vol. 271, pp. 213–23.
39. Y.S. Sato, S.H.C. Park, and H. Kokawa: *Metall. Mater. Trans. A*, 2001, vol. 32A, pp. 3033–42.
40. Y.S. Sato, H. Kokawa, M. Enomoto, and S. Jogan: *Metall. Mater. Trans. A*, 1999, vol. 30A, pp. 2429–37.
41. P. Heurtier, M.J. Jones, C. Desrayaud, J.H. Driver, F. Montheillet, and D. Allehaux: *J. Mater. Proc. Technol.*, 2006, vol. 171, pp. 348–57.
42. Z. Marciniak and K. Kuczynski: *Int. J. Mech. Sci.*, 1967, vol. 9, pp. 609–20.
43. ASM International Handbook Committee: *ASM Handbook*, vol. 12, *Fractography*, ASM INTERNATIONAL, Materials Park, OH, 1987.
44. P. Cavaliere, A. Squillace, and F. Panella: *J. Mater. Proc. Technol.*, 2008, vol. 200, pp. 364–72.
45. W. Xu, J. Liu, G. Luan, and C. Dong: *Mater. Des.*, 2009, vol. 30, pp. 1886–93.
46. K. Elangovan and V. Balasubramanian: *Mater. Charact.*, 2008, vol. 59, pp. 1168–77.
47. J.J. Shen, H.J. Liu, and F. Cui: *Mater. Des.*, 2010, vol. 31, pp. 3937–42.
48. H. Liu, J. Shen, Y. Huang, L. Kuang, C. Liu, and C. Li: *Sci. Technol. Weld. Join.*, 2009, vol. 14, pp. 577–83.
49. P. Cavaliere, A.D. Santis, F. Panella, and A. Squillace: *Int. J. Fatigue*, 2009, vol. 31, pp. 385–92.
50. S. Hong, S. Kim, C.G. Lee, and S.-J. Kim: *Scripta Mater.*, 2006, vol. 55, pp. 1007–10.